Investigation of new routes for the preparation of mesoporous calcium oxide supported nickel materials used as catalysts for methane dry reforming reaction

Ola El Samrout, Leila Karam, Karam Jabbour, Pascale Massiani, Franck Launay, Nissrine El Hassan

Investigation of new routes for the preparation of mesoporous calcium oxide supported nickel materials used as catalysts for methane dry reforming reaction

Ola El Samrout,[a,b] Leila Karam,[a,b] Karam Jabbour,[a] Pascale Massiani,[b] Franck Launay*[b] and Nissrine El Hassan*[a]

[a] University of Balamand, Faculty of Engineering, Department of Chemical Engineering, P.O. Box 33, Amioun El Koura, Lebanon.
[b] Sorbonne Université, CNRS UMR 7197, Laboratoire de Réactivité de Surface, LRS, Campus Pierre et Marie Curie, 4 Place Jussieu, F-75005 Paris, France.
*Corresponding authors: franck.launay@sorbonne-universite.fr (F. Launay) and nissrine.hassan@balamand.edu.lb (N.El Hassan)

Abstract

Nowadays, one of the metal oxides attracting significant attention in catalysis is calcium oxide (CaO) due to the fact that it is cheap, environmentally friendly and is characterized by a strong basic character. These distinctive properties make CaO promising in a wide range of industrial applications such as light alkane dehydrogenation, oxidation of methanol and carbon capture and storage. CaO is commonly synthesized by adopting methods of preparation that are expensive, complicated or require high temperature and pressure, and that result usually in non-ordered structures with low specific surface area. In this work, CaO support was synthesized following three synthetic approaches: i) a new template-free synthesis involving mesoporous calcium carbonate, an analog of Upsalite ($MgCO_3$) as precursor, ii) a hard template protocol using silica SBA-15 to replicate CaO, reported for the first time in literature for this oxide and, iii) a hydrothermal autoclave approach using PEG 1500 or CTAB as structure directing agents. Nickel was introduced up to 10 wt.% by either "two-solvents" post-impregnation or by a "one pot" method. All calcined materials were characterized by nitrogen physisorption, X-Ray diffraction (XRD), H_2 temperature programmed reduction (TPR), thermogravimetric analysis (TGA) and transmission electron microscopy (TEM). After in-situ reduction with H_2, the reactivity of all CaO-based catalysts was evaluated in the reaction of dry reforming of methane (DRM) carried at 650 °C, during 13 h (stability test) and under a gas hourly space velocity of 36 $L.g_{cat}^{-1}.h^{-1}$. In this catalytic reaction, which aims the production of synthesis gas (H_2 + CO), both basicity and porous properties are important criteria to prevent catalysts deactivation by coke deposition/accumulation and/or sintering of active phase. The present results show that the template-free and hard template based synthesis routes are successful in yielding active, stable and selective Ni-CaO catalysts for DRM. The former represents an easy, scalable, time saving and low energy synthetic approach whereas the latter results in higher metal support interaction, which helps limiting metal sintering and improving resistance towards coke formation on stream.

Introduction

Currently, metal oxides are attracting a significant deal of attention owing to their distinctive properties, low cost and wide range of potential applications.[1,2] Among them, metal oxides of the alkaline earth family, and especially MgO and CaO, display great potential in a wide range of industrially-oriented applications such as adsorption and catalysis. The main utilization of CaO resides in isomerization of alkenes and oxidative dehydrogenation[3-5] but CaO is also involved in $CaO/CaCO_3$ looping processes which are cheap and energy efficient techniques for carbon capture and storage. This oxide can be efficiently regenerated and re-used for several looping cycles while keeping high number of oxygen vacancies required for chemical looping. Regardless of its industrial benefits, the CaO-based looping technique offers environmental

interests since spent CaO is chemically inert and rather than being disposed in the environment, it can be adopted as a raw material in cement production.[6]

Alkaline earth metal oxides, especially MgO, have also an important role in the dry reforming of methane (DRM) application that is a promising route toward a cleaner environment. This catalytically activated reaction produces syngas, a key intermediate for greener chemical processes and energy sources, while simultaneously consuming two major greenhouse gases (CH_4 and CO_2).[7] Despite the advantages of DRM, its industrialization is limited due to frequent catalysts deactivation related to sintering and solid carbon deposition. This is why continuous efforts are devoted to the design of more resistant catalysts capable of operating stably for long catalytic runs. As well established in the literature, deactivation can be prevented by (i) synthesizing very small and well dispersed metallic active sites, (ii) establishing a strong metal-support interaction and (iii) introducing an element with a high capability of carbon removal.[8-15] To this respect, using alkaline earth metal oxides as catalytic supports in DRM allows to benefit from their high oxygen storage capacities. Hence, such basic oxides are able to decrease carbon buildup on active metal surface by providing kinetically larger concentration of labile oxygen that is known to contribute to the removal of carbonaceous deposits by initiating their oxidation.[16] It is noteworthy that, compared to other metal oxides, the usage of CaO in reforming reactions is still very scarce despite promising reported outcomes. For instance, the addition of CaO up to 20 wt.% in a Ni/CaO-Al_2O_3 catalyst with 6 $m^2\ g^{-1}$ of surface area was proven to increase the stability of the resulting material and its resistance to coke deposition in DRM.[17]

However, the benefits of adding CaO are not systematic. Indeed, it was shown that a non-porous NiO-impregnated CaO material with 8 $m^2\ g^{-1}$ of surface area was not stable when tested in DRM for five successive cycles. The hydrogen production drastically decreased from 42% in the first cycle (after 20 min at 600 °C) to 23% in the fifth cycle (carried out at 700 °C).[18] Similarly, a NiO-CaO catalyst with a Ni/Ca ratio equal to 3 and a surface area of 2 $m^2\ g^{-1}$ showed a drastic decrease in CH_4 and CO_2 conversions after only 1 h of reaction carried out at 850 °C with a GHSV of 11.5 L $g_{cat}^{-1}\ h^{-1}$, and the carbon deposit was estimated to be about 26 wt.%.[19] Carbon formation was estimated as high as 44 wt.% in the case of a 10 wt.% Ni/CaO with a surface area of 15 $m^2\ g^{-1}$ prepared by the sol-gel technique and used in DRM at 700 °C and a GHSV of 48 L $g_{cat}^{-1}\ h^{-1}$.[20] In all these examples, it can be noticed that the materials exhibit very small external surface area, while high surface area is necessary for high nickel dispersion and prevention against coke nanotubes formation. Hence, a target to improve such type of catalysts for DRM could be to obtain CaO supports with increased porosity and surface area.

The preparation of such metal oxides is commonly envisaged by using either soft templates, hard templates or simply thermal treatment (calcination) of a metal precursor. For the soft template approach, ordered CaO oxides were produced via a surfactant-assisted hydrothermal synthesis using CaO powders as the inorganic source and an amphiphilic molecule such as hexadecyltrimethylammonium bromide (CTAB), poly(ethylene)glycol (PEG), or triblock polymers made of poly(ethylene oxide) (PEO) and poly(propylene oxide) (PPO) (e.g. P123).[5,21] Such CaO supports obtained in presence of surfactant exhibit mesoporous structures with high surface areas that are (sometimes) accompanied by a macroporous

character. By adopting a spray-drying synthesis method with an inorganic NaCl salt as template and calcium D-gluconate monohydrate as precursor, an ordered CaO sorbent with a surface area in the range of 23 $m^2 g^{-1}$ could be produced.[22] Besides, the sol-gel method was described to afford CaO sorbents with micro-mesoporous channels (surface area equals to 12 $m^2 g^{-1}$) upon using Ca nitrate and CTAB, the latter serving both as template and stabilizing agent for controlling the CaO particle sizes as well as for preventing their agglomeration.[6] Furthermore, a citrate-assisted sol-gel technique was adopted using Ca acetate monohydrate as precursor and P123 as surfactant. The resulting CaO material was reported to be porous with wide pores size distribution (PSD) and a surface area of 20 $m^2 g^{-1}$.[23]

The hard template approach (also known as nanocasting) is more often used for the preparation of porous metal oxides including ordered alkaline earth metal oxides such as MgO. To the best of our knowledge, such synthesis pathway was not yet adopted for synthesizing CaO. However, as reported earlier, ordered mesoporous MgO with a high surface area (150 $m^2 g^{-1}$) and a narrow pore volume distribution (peak at around 0.73 $cm^3 g^{-1}$, small standard deviation away from the maxima) could be obtained using Mg nitrate and carbon aerogel as hard template that is subsequently removed by combustion at 600 °C for 8 h.[24] MgO with a higher specific surface area (280 $m^2 g^{-1}$) was also prepared by substituting the carbon aerogel template by CMK-3, itself synthesized using mesoporous SBA-15 silica as hard template.[25]

In comparison to soft and hard template approaches, thermally treating a calcium precursor is recognized as the simplest and the most time efficient strategy. Regarding the available literature, a CaO material used for CO_2 sorption, with a specific surface area of 11 $m^2 g^{-1}$ and a pore volume of 0.053 $cm^3 g^{-1}$, was simply prepared via calcination of the commercially available calcium acetate monohydrate salt at 750 °C, for 4 h, under a controlled heating rate of 3 °C min^{-1}.[26] Besides, other commercial calcium precursors such as calcium hydroxide, calcium carbonate and calcium oxalate monohydrate were also tested. In these examples, the calcination treatment was carried out at elevated temperatures ranging from 800 to 900 °C and a slow heating rate of 1.5 °C min^{-1} for short time affording CaO with specific surface areas from 5 to 25 $m^2 g^{-1}$ (depending on the used calcium precursor) for application in transesterification.[27-29] Some authors reported that microporous CaO having surface areas of 6 or 9 $m^2 g^{-1}$, for CO_2 sorption, could be respectively obtained by calcination of either calcium oxalate or calcium 2-ethylhexanoate at 900 °C for 1 h.[30] On the other hand, macroporous CaO were obtained by thermal decomposition of calcium propionate or calcium acetate, yielding solids with surface areas close to 15 or 20 $m^2 g^{-1}$ and a particle sizes distributions with maxima at 230 or 125 nm, respectively.[30]

Moreover, it is worth mentioning that porous CaO materials are often described as micro-mesoporous and macroporous samples although their textural properties and N_2-sorption isotherms might not be falling in the conventional (standard) range and shape expected. We tentatively ascribe this to the fact that synthesizing porous CaO is complex. Indeed, a desired structure might not be obtained even when adopting a protocol that was shown to be efficient for the synthesis of porous MgO (or even other oxides). Thus, the assembly of porous CaO solids is a critical challenge faced by the development of CaO-based catalysts for wider applications such as syngas production by means of methane reforming. Limited are

the studies dealing with application of CaO as support for Ni (a transition metal that is active in methane reforming) species in DRM.[18-20] Using CaO with a structured porous network as support for Ni nanoparticles could result in beneficial outcomes since the characteristics of the carrier could play a crucial role in (i) metal dispersion, (ii) reaction initiation, (iii) deactivation resistance and (iv) stability preservation.

In this context, the aim of the present work is (i) to enrich the available literature on porous CaO by adopting three different pathways (two of which were never considered before) for their synthesis, (ii) to evaluate the effect of the preparation method on the role of CaO as catalyst support for Ni species in methane dry reforming and, (iii) to provide an *in depth* understanding of the factors that lead to the design of stable CaO-based catalysts for *syn*gas generation by adopting various Ni introduction routes. In a first approach, CaO will be synthesized using a novel template-free synthesis method based on the thermal decomposition of ordered porous calcium carbonate prepared under a CO_2-rich atmosphere, at room temperature and atmospheric pressure. $CaCO_3$ of the Upsalite type,[31-35] i.e. a particular family of micro-mesoporous magnesium and calcium carbonate powders, will be used as precursor. Such conversion of porous $CaCO_3$ into CaO represents a new, easy, scalable, template-free, time and energy efficient method. Second, a nanocasting (hard template) method based on the usage of mesostructured porous silica (SBA-15) as parent template will be tested to synthesize porous CaO. Preparing CaO following this approach is also considered to be a new pathway, never applied previously to our knowledge. The third and last method adopted resides in the preparation of CaO by a soft-template approach involving a hydrothermal treatment and using two different families of surfactants. This last strategy, inspired from literature, afforded CaO solids for comparison purposes. For the sake of completion, the active phase (widely available and cheap Ni salts) will be introduced by either using a "two-solvents" post-impregnation method[36] or by a direct "one pot" methodology, i.e. during the CaO precipitation. These procedures will be compared based on the physico-chemical characteristics and catalytic performances of the obtained samples, searching for the optimum Ni introduction along with CaO preparation routes leading to the most efficient catalyst.

Experimental Procedures

Materials preparation

Template-free Synthesis (TF) (one pot: 5, 7.5 and 10 wt.% Ni)

In a round-bottom flask of 250 mL, 4.55 g of calcium hydroxide powder ($Ca(OH)_2$, Sigma Aldrich, 1305-62-0) were mixed with 76.68 mL of absolute ethanol (CH_3CH_2OH, Sigma Aldrich, 64-17-5) and 23.32 mL of ethylene glycol ($HOCH_2CH_2OH$, 99.8 %, Sigma Aldrich, 107-21-1), which corresponds to a 3/7 weight ratio of ethylene glycol over absolute ethanol. Then a flow of CO_2 (0.21 L min^{-1}) was allowed to bubble for a few minutes into the mixture, at room temperature (RT) and under stirring, to provoke the carbonation of all dissolved $Ca(OH)_2$. Using centrifugation, the small amount of unreacted solid was discarded, and the transparent supernatant was divided equally among 3 beakers. A given weight of Ni nitrate hexahydrate ($Ni(NO_3)_2.6H_2O$, Sigma Aldrich, 13478-00-7) was added in each of them, calculated as to get 5,

7.5 and 10 wt.% Ni in the final solid and considering the amount of CaO resulting from the decomposition of $CaCO_3$ by calcination. Each mixture was left for aging at RT under slow stirring, leading to the progressive formation of a gel then crystals. After 48 h, the obtained cloudy green solutions, whose color deepened with increasing the Ni content, were centrifuged, and the solids were recovered and dried under vacuum overnight at RT. The powders were then subjected to calcination in air at 850 °C for 3 h at a rate of 0.5 °C min^{-1} in order to convert $CaCO_3$ into CaO and obtain NiO.[37] These TF synthesized one pot calcined samples are referred to as $Ni_{5(OP)}/CaO_{TF}$, $Ni_{7.5(OP)}/CaO_{TF}$ and $Ni_{10(OP)}/CaO_{TF}$. For the sake of completion, a Ni-free $CaO_{(TF)}$ sample was also prepared following this route but without Ni addition.

Hydrothermal Autoclave Synthesis (HA) (one pot: 5 wt.%Ni using either PEG or CTAB)

Polyethylene glycol PEG1500 ($H(OCH_2CH_2)_nOH$, Sigma Aldrich, 25322-68-3) or hexaldecyltrimethyl ammonium bromide CTAB ($CH_3(CH_2)_{15}N(Br)(CH_3)_3$, Sigma Aldrich, 57-09-0) were used as structure directing agents. First, 1.55 g of PEG1500 (resp. 7.79 g of CTAB) were dissolved in 64 mL (resp. 45 mL) of distilled water under stirring. After 15 min, 1.12 g of calcium oxide powder (CaO, Sigma Aldrich, MW= 56.08 g mol^{-1}, 1305-78-8) were added and the solution was kept under stirring for 0.5 h until complete dissolution. An ultrasonic treatment was then applied at RT for at least 4 h. After that, the solution was transferred to a Teflon lined stainless steel autoclave having a packed volume of 85 mL and was placed in a hydrothermal oven at 240 °C for 72 h. The obtained mixture was filtered and the solid was washed using about 60 mL of distilled water then ethanol for several times in order to remove the majority of the surfactant. The intermediate $Ca(OH)_2$ formed at this stage was dried for 12 h at 55 °C. To ensure a complete conversion of $Ca(OH)_2$ into CaO, the resulting powder was next subjected to calcination in a tubular furnace under an oxygen flow of 80 mL min^{-1} at 550 °C for 3 h at a rate of 1 °C min^{-1}. The obtained supports were denoted $CaO_{(HA\text{-}PEG)}$ and $CaO_{(HA\text{-}CTAB)}$. The $Ni_{5(OP)}/CaO_{(HA\text{-}PEG)}$ and $Ni_{5(OP)}/CaO_{(HA\text{-}CTAB)}$ samples were prepared following the same hydrothermal autoclave synthesis method except for the addition of an adequate amount of nickel nitrate hexahydrate ($Ni(NO_3)_2.6H_2O$, Sigma Aldrich, 13478-00-7) in the gel, made simultaneously to the addition of the CaO powder, before the hydrothermal treatment, and corresponding to 5 wt.% Ni in the calcined material.

Hard Template Synthesis (HT) (post impregnation: 10 wt.% Ni)

A protocol used in one of our previous study[38] was adapted. Briefly, 1 g of dry commercial mesostructured silica (Sigma Aldrich, product number # 7631-869) was suspended in 35 mL of n-hexane under stirring (velocity of 125 rpm) for 15 min. Then, stirring was stopped and an aqueous solution of calcium nitrate tetrahydrate 0.552 g mL^{-1} ($Ca(NO_3)_2.4H_2O$, Sigma Aldrich, product number # 13477-344) was added dropwise. The impregnation was carried out in such a way that the volume of the added aqueous solution was equal to the pore volume of the support (as determined by N_2 sorption experiments, see below). The impregnation procedure was repeated five times until the pore volume of the resulting material decreased to c.a. 65% of the original volume of SBA-15. After each impregnation, the hexane suspension was filtered and the solid recovered was left to dry at RT for at least 24 h (evaporation of n-hexane and water) and was slowly calcined in air (thin bed) at 450 °C for 5 h at a heating rate

of 0.5 °C min^{-1}.[39] After completing all calcium impregnations, the silica template was removed by dissolution in a basic 2 M solution of sodium hydroxide (NaOH, Sigma Aldrich, product number # 1310-732) at RT. Silica dissolution was conducted as follows: 1 g of the calcined calcium-impregnated SBA-15 was mixed with 20 mL of the NaOH solution for 1 h followed by centrifugation (rotation speed fixed at 2500 rpm) for 0.75 h at 25 °C. Silica removal was repeated several times (to insure complete dissolution of SiO_2) before cleaning the powder with distilled water. The resulting calcium oxide obtained from this method is denoted $CaO_{(HT)}$. The deposition of Ni onto $CaO_{(HT)}$ was carried out by the "two-solvents" impregnation method, done as follows: after suspending the support in n-hexane (rotation speed: 125 rpm, duration: 0.25 h), an aqueous solution of Ni nitrate hexahydrate ($Ni(NO_3)_2.6H_2O$, Sigma Aldrich, 13478-00-7) prepared as to obtain a 10 wt.% Ni loading in the final solid, was added dropwise to the static suspension. After drying at RT, calcination (in air) was conducted at 450 °C for 5 h at a heating rate of 0.5 °C min^{-1}. The resulting sample was designated as $Ni_{10(TS)}/CaO_{(HT)}$.

Characterization techniques

- **N_2 sorption -** Textural properties were determined from nitrogen adsorption-desorption isotherms using an ASAP 2020 Micrometritic apparatus. Prior to analysis, the sample (50-80 mg) was degassed at 250 °C for 2 h under vacuum. Surface areas were estimated by applying the BET method in the relative P/P_0 pressure range of 0.05 to 0.25. They were expressed in m^2 per gram of sample referring to a monolayer adsorption of the N_2 gas on the surface by Van der Wall forces. Total pore volumes were determined from the N_2 adsorption value at a relative pressure of 0.99. Pore size distributions were measured using the Barrett-Joyner-Halenda (BJH) method applied on the desorption isotherm.

- **X-ray Diffraction (XRD) -** Crystalline structures were identified from X-ray diffraction patterns recorded on a PANalytical X'Pert diffractometer using a Cu Kα (λ=1.5405 Å) radiation source and working at 30 mA and 40 kV. The diffractograms were recorded for 2Θ angles ranging from 10 to 90°, with a step size of 0.05° and 1 s time per step. Crystal phases were established by reference to the international center for diffraction data (ICDD). Mean crystallite sizes were estimated by applying the Scherrer's equation: $D = (K\lambda/ \beta\cos\Theta)$ where D represents the particle size, K is a constant equal to 0.9, Θ refers to the position of the diffraction peak, λ is the X-Ray wavelength and β is the full width at half maximum (FWHM) of the peak.

- **Temperature Programmed Reduction (TPR) -** Reducibility of calcined materials was studied using an Autochem 2920 Micromeritics apparatus supplied with a thermal conductivity detector (TCD). The sample (50-80 mg) was introduced on quartz wool in a U-shaped quartz tube and submitted to heating from RT to 900 °C at a constant rate of 10 °C min^{-1} in the presence of a reducing 5 vol.% H_2/Ar flow (30 mL min^{-1}). Prior to TCD detection, the gas flow was directed toward a cold trap (placed in a bath of ice and NaCl) in order to trap any water formed during reduction and ensure that the TCD signal only corresponds to hydrogen consumption. Total hydrogen uptake (H_2-uptake) was measured by integrating the area under the plot of the TCD signal versus temperature and used to evaluate the percentage of nickel in each sample from the following equation:

$$wt.\%\ Ni = \frac{H_2\ uptake\ (L\ g^{-1}) \times MwNi\ (\mathrm{g}\ mol^{-1})}{22.4\ (\mathrm{L}\ mol^{-1})}$$

- **Transmission Electron Microscopy (TEM) -** Ultrathin transmission electron microscopy (TEM) observations were done to determine the morphology of the fresh and spent catalysts and visualize the Ni nanoparticles and coke deposits (in the spent catalysts) both inside and outside the pores of the CaO supports. The observations were done on a JEOL-JEM 200 electron microscope (LaB_6 gun) working at 200 keV and equipped with energy dispersive X-ray spectroscopy (EDXS).

- **Thermogravimetric Analysis (TGA-DTG) -** The amounts of carbon deposition in the spent catalysts, expressed in weight percent, were obtained on a TA SDT Q600 thermal analyzer apparatus. The experiments were carried out under an air flow (100 mL min^{-1}) while heating the samples from room temperature to 900 °C at a rate of 10 °C min^{-1} and recording the evolution with time of weight loss (TGA). DTG curves were obtained by derivation of TGA profiles.

Reactivity Measurements

Catalytic performances were measured after reduction of the prepared materials, using a Microactivity catalytic reactor (MAR from PID ENG & TECH Spain) and applying reaction conditions chosen from our previous works.[10-13] 100 mg of each calcined sample was loaded between 2 layers of quartz wool in the reactor. A leak test was first accomplished in the presence of an inert gas (argon), then reduction of the sample was operated at atmospheric pressure under flowing 5%H_2/Ar (30 mL min^{-1}) and increasing the temperature from room temperature up to 700 °C and keeping this temperature for 2 h to ensure full nickel oxide reduction into Ni^0. The temperature was then decreased to 650 °C to conduct the activity and stability test for about 13 h, at atmospheric pressure, under a CH_4:CO_2 ratio of 1:1 (diluted in 90% Ar) and a gas hourly space velocity GHSV of 36 L g_{cat}^{-1} h^{-1}. The gaseous effluents were analyzed using an INFICON 3000 Micro-GC equipped with a TCD and 2 parallel columns, one filled with a molecular sieve for the detection of H_2, CH_4 and CO, and a plot-U one that serves for the detection of CO_2. The conversions of CH_4 and CO_2 as well as the H_2:CO ratio were calculated as follows:

$$X\ CH_4\ (\%) = \frac{\mathrm{CH_4}_{\ in} - \mathrm{CH_4}_{\ out}}{\mathrm{CH_4}_{\ in}} * 100$$

$$X\ CO_2\ (\%) = \frac{\mathrm{CO_2}_{\ in} - \mathrm{CO_2}_{\ out}}{CO_{2in}} * 100$$

$$H_2{:}\,CO\ ratio = \frac{\text{mol of } H_2 \text{ produced}}{\text{mol of CO produced}}$$

The obtained conversion values were next used to calculate apparent conversion rates for each reactant, expressed as number of moles converted per second and per gram of nickel:

$$r(CH_4) = \frac{Flow\ rate\ of\ CH_4\ (mmol.s^{-1}) \times CH_4\ conversion}{weight\ of\ catalyst\ (g) \times\ Ni\ wt.\%}$$

$$r(CO_2) = \frac{Flow\ rate\ of\ \ CO_2\ (mmol.s^{-1}) \times CO_2\ conversion}{weight\ of\ catalyst\ (g) \times\ Ni\ wt.\%}$$

A blank test (without catalyst) was conducted, confirming the absence of conversion for both CH_4 and CO_2 reactants, ensuring that all observed activity comes only from the catalysts.

Results and discussions

This work aimed at designing porous calcium oxides well-adapted to be used as supports of catalytically active and stable Ni nanoparticles for the very demanding reaction of dry methane reforming. Despite their strong interest, such materials have been poorly described in the literature due to their difficult synthesis. The grain morphology of the support and its textural properties should influence the dispersion of nickel and thus indirectly the performance of the catalysts. In this contribution, we investigate three different synthetic pathways and study six materials. Three of them, $Ni_{5(OP)}/CaO_{(TF)}$, $Ni_{7.5(OP)}/CaO_{(TF)}$ and $Ni_{10(OP)}/CaO_{(TF}$), with Ni loadings from 5 to 10 wt.%, were synthesized following a template-free synthesis protocol (TF) adapted from the works of Yamanaka et al.[28,35] Two other samples ($Ni_{5(OP)}/CaO_{(HA\text{-}CTAB)}$ and $Ni_{5(OP)}/CaO_{(HA\text{-}PEG)}$), with 5 wt.% Ni incorporated by a one pot strategy, were prepared using a hydrothermal autoclave synthesis (HA) based on a surfactant-assisted dissolution-recrystallization method inspired by the works of Liu et al.[21] and Deng et al.[5], which was slightly altered by using either polyethylene glycol (PEG) or hexaldecyltrimethyl ammonium bromide (CTAB). The last sample ($Ni_{10(TS)}/CaO_{(HT)}$) was obtained following a hard template synthesis route (HT) based on a repeated post-impregnation of porous SBA-15 with an aqueous Ni salt solution. To the best of our knowledge, such hard template preparation of CaO using mesoporous SBA-15 and the "two-solvents" impregnation method is not yet reported in the literature and we chose the synthesis conditions according to a previous study dealing with nanocasting of cobalt and other metals within porous SBA-15.[36]

Textural properties of calcined samples

The textural properties of the calcined materials were determined from N_2-sorption measurements. The obtained isotherms are plotted in Fig. 1 and the corresponding textural data are gathered in Table 1. With the exception of the HT (Hard Template) series, nickel was introduced during the synthesis of the CaO support itself.

All adsorption-desorption profiles exhibit type II isotherms with sometimes a H_3 hysteresis loop, characteristic of solids with large pore opening, typical of macroporous materials.[40] The

Sample	Exp. Ni content (wt%)	Specific surface [a] ($m^2\ g^{-1}$)	Pore volume [a] ($cm^3\ g^{-1}$)	Temp. of main peaks [b] (°C)	Total H_2-uptake [b] ($mL\ g^{-1}$)	$Ø_{NiO}$ [c] (nm)	$Ø_{CaO}$ [c] (nm)	$Ø_{Ni0}$ [d] (nm)	$Ø_{CaCO3}$ [d] (nm)
$CaO_{(TF)}$	-	15	0.04	-	-	-	100	-	-
$Ni_{5(OP)}/CaO_{(TF)}$	5	11	0.02	600	19	21	148	15	57
$Ni_{7.5(OP)}/CaO_{(TF)}$	7.5	12	0.03	455, 600	29	26	n.d.	18	35
$Ni_{10(OP)}/CaO_{(TF)}$	10	12	0.02	465, 600	38	30	70	21	63
$CaO_{(HT)}$	-	85	0.58	-	-	-	n.d. [e]	-	-
$Ni_{10(TS)}/CaO_{(HT)}$	10	103	0.49	650, 800	38	4	n.d. [e]	6-8	n.d. [e]
$CaO_{(HA\text{-}PEG)}$	-	31	0.08	-	-	-	17	-	-
$Ni_{5(OP)}/CaO_{(HA\text{-}PEG)}$	5	25	0.07	350, 520, 620	19	12	18	55	45
$CaO_{(HA\text{-}CTAB)}$	-	50	0.10	-	-	-	14	-	-
$Ni_{5(OP)}/CaO_{(HA\text{-}CTAB)}$	5	45	0.11	335, 460, 660	-	9	15	109	62

a: specific surfaces and total pores volumes deduced from N_2 sorption isotherms
b: temperatures of maxima of main peaks and total H_2 consumption during TPR
c, d: mean sizes of the crystalline domains in the (c) calcined and (d) spent materials calculated using the Scherrer's equation applied to a characteristic peak at 2Θ around 63° (NiO), 32° (CaO), 44° (Ni^0) and 29° ($CaCO_3$) ; n.d. for not detected

increase in the quantity of adsorbed nitrogen appearing at low P/P_0 values refers to the

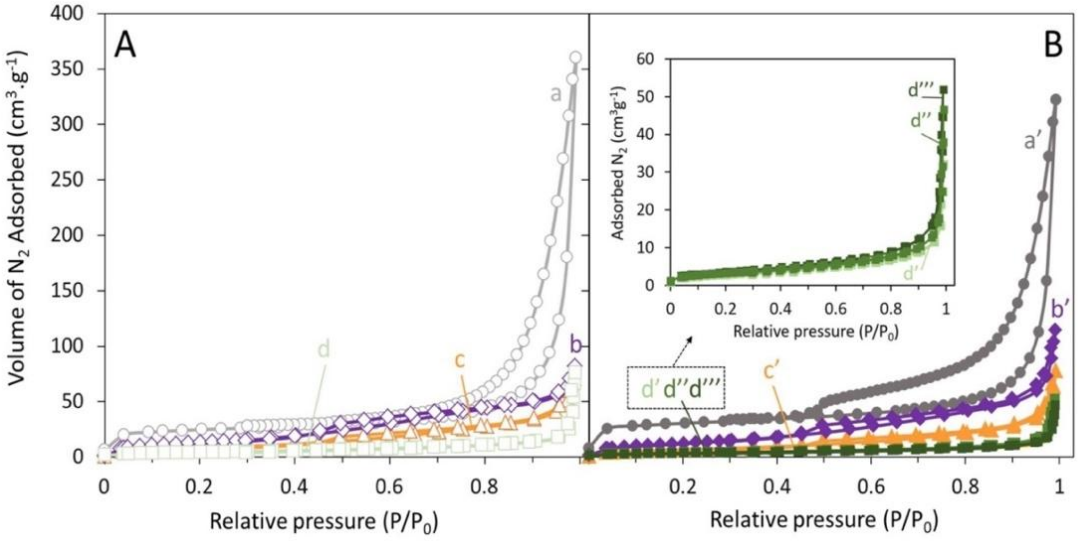

Figure 1: N_2 adsorption-desorption isotherms (77 K) of the (A) CaO supports and (B) Ni-CaO synthesized samples obtained by hard template method (a) $CaO_{(HT)}$ and (a') $Ni_{10(TS)}/CaO_{(HT)}$; hydrothermal autoclave synthesis (b) $CaO_{(HA\text{-}CTAB)}$, (b') $Ni_{5(OP)}/CaO_{(HA\text{-}CTAB)}$, (c) $CaO_{(HA\text{-}PEG)}$ and (c') $Ni_{5(OP)}/CaO_{(HA\text{-}PEG)}$; template-free syntheses (d) $CaO_{(TF)}$ (d') $Ni_{5(OP)}/CaO_{(TF)}$, (d'') $Ni_{7.5(OP)}/CaO_{(TF)}$, (d''') $Ni_{10(OP)}/CaO_{(TF)}$.

Table 1: Textural properties of calcined samples, temperature and H_2-uptake during reduction, and average size of crystalline domains in fresh and spent catalysts

completion of the monolayer coverage whereas the non-limited increase of adsorbed N_2 at P/P_0 values around 1.0 reveals an unrestricted monolayer-multilayer adsorption potentially associated to the presence of inter-particle porosity. Such behavior could be attributed to the existence of non-rigid aggregates of slit-shaped particles presenting edges such as those detected in cubic-shape particles.[40-43] Moreover, the appearance of the hysteresis loop on most of the isotherms in the relative pressure range between 0.5 to 1.0 indicates the presence of (some) smaller pores (such as mesopores) within calcined samples.

According to N_2-sorption isotherms, the samples prepared by the hard template (nanocasting) protocol are characterized by a higher degree of mesoporosity compared to the other ones. In fact, the Ni-free $CaO_{(HT)}$ synthesized by this method exhibits the highest BET surface area (85 $m^2\ g^{-1}$) amongst the CaO supports (Table 1), and its porous structure appears more regular and better organized than those of the other CaO materials (Fig. 1A). According to recent literature, nanocasting applied to the synthesis of MgO resulted in mesoporous solids with high surface areas (150 and 280 $m^2\ g^{-1}$).[24,25] To date, this approach has not been yet used for the preparation of CaO-based materials. Hence, the surface area as high as 85 $m^2\ g^{-1}$ ($CaO_{(HT)}$) and even 103 $m^2\ g^{-1}$ ($Ni_{10(TS)}/CaO_{(HT)}$) obtained here for the samples prepared by this route (Table 1), significantly higher than all previously reported values for CaO-based solids,[6,22,23,27-30] demonstrate its potential to prepare high surface area calcium oxide based materials. In contrast, the template-free method associated to direct introduction of Ni in the synthesis gel led to a series of materials (with 5 to 10 wt.% of Ni) with similar but very low BET surface area, that seem to be independent of the Ni loading (c.a. 12 $m^2\ g^{-1}$ for Ni containing solids vs. 15 $m^2\ g^{-1}$ for CaO alone, Table 1). These values are in the range of those between 6 and 11 $m^2\ g^{-1}$ reported in the literature for CaO obtained by template-free method and prepared by calcination within the same range of temperature (i.e. 800-900 ºC) of other precursors.[26-30]

Regarding the samples prepared by hydrothermal autoclave synthesis, it is clear that the nature of the structure directing agent (SDA) had an effect on both the BET surface area and pore volume of the resulting material. Thus, using CTAB instead of PEG resulted, after treatment at 240 °C for 72 h, in a CaO support with higher BET surface area (50 vs 31 $m^2\ g^{-1}$) and a slightly higher pore volume (0.10 vs 0.08 $cm^3\ g^{-1}$). Again, these values are higher than those between 12 and 20 $m^2\ g^{-1}$ for CaO materials synthesized by soft template methods in the literature.[6,22,23] Similarly, $Ni_{5(OP)}/CaO_{(HA\text{-}CTAB)}$ exhibits a higher surface area (45 vs 25 $m^2\ g^{-1}$) and a higher pore volume (0.11 vs 0.07 $cm^3\ g^{-1}$) than $Ni_{5(OP)}/CaO_{(HA\text{-}PEG)}$. As a whole, it is worth to note that, in addition to their very low number, the existing publications on Ni/CaO materials[18,19] report surface area in the range 2 to 12 $m^2\ g^{-1}$, always below those from 12 to 103 $m^2\ g^{-1}$ found for the Ni/CaO prepared in the present work.

Structural properties of calcined samples

Representative wide-angles XRD patterns of calcined samples are shown in Fig. 2A. The average CaO and NiO particle sizes deduced from the patterns are listed in Table 1. The XRD peaks observed at 2Θ equal to 32, 36, 37, and 54° are assigned to crystalline CaO with a cubic structure (JCPDS 01-082-1691). For the samples prepared by template-free synthesis (e.g. $Ni_{10(OP)}/CaO_{(TF)}$, Fig. 2A, curve d), these peaks are relatively sharp, indicating high crystallinity as well as presence of large CaO crystallites (70-148 nm, Table 1). The peaks are less intense and broader in the patterns of both $CaO_{(HA\text{-}CTAB)}$ and $Ni_{5(OP)}/CaO_{(HA\text{-}CTAB}$ (Fig. 2A, curve b) issued from hydrothermal autoclave synthesis in the presence of CTAB as SDA, revealing much smaller calcium oxide nanoparticles (14-15 nm, Table 1), also slightly smaller than those in $CaO_{(HA\text{-}PEG)}$ and $Ni_{5(OP)}/CaO_{(HA\text{-}PEG)}$ (Fig. 2A, curve c) synthesized using PEG (17-18 nm, Table 1). On the other hand, it is noteworthy that the average CaO sizes are very small (below the detection limit of the apparatus), unless CaO is amorphous, in $CaO_{(HT)}$ and $Ni_{10(TS)}/CaO_{(HT)}$ (Fig. 2A, curve a), both obtained by using SBA-15 as a hard template.

The XRD peaks detected at 2Θ equal to 43, 52, 63 and 68° for most of the Ni-containing samples correspond to NiO nanoparticles with a cubic structure (JCPDS 01-078-0643 file). In the $Ni_{x(OP)}/CaO_{(TF)}$ series prepared by template-free synthesis ($Ni_{5(OP)}/CaO_{(TF)}$, $Ni_{7.5(OP)}/CaO_{(TF)}$ and $Ni_{10(OP)}/CaO_{(TF)}$), the mean size of the crystalline NiO domains increases as expected with the Ni content and the sizes are rather big (from 21 to 30 nm, Table 1), in agreement with the limited specific surfaces that make nickel dispersion more difficult. TEM images of $Ni_{5(OP)}/CaO_{(TF)}$ and $Ni_{10(OP)}/CaO_{(TF)}$ visualize the enrichment in NiO nanoparticles on the CaO surface when more Ni is present (Fig. 3 A, B).

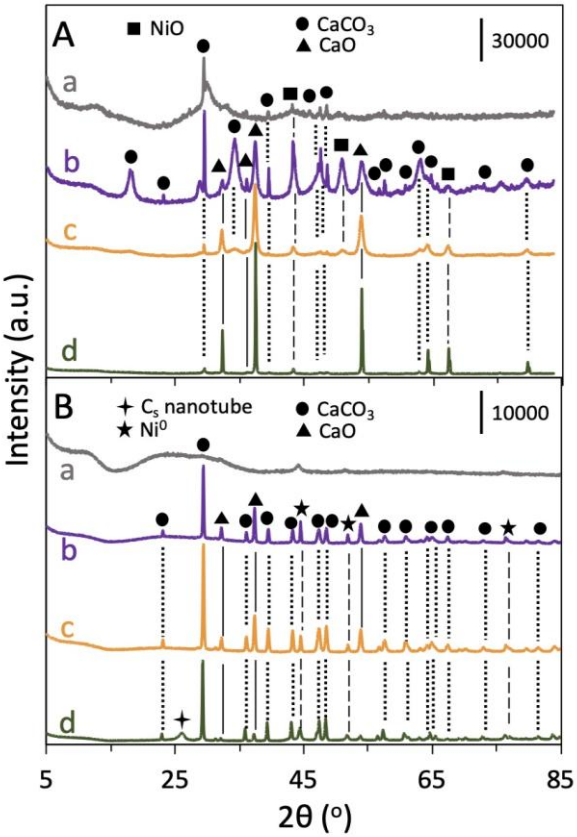

Figure 2: Wide-angles XRD patterns of (A) calcined and (B) spent samples: (a) $Ni_{10(TS)}/CaO_{(HT)}$, (b) $Ni_{5(OP)}/CaO_{(HA\text{-}CTAB)}$, (c) $Ni_{5(OP)}/CaO_{(HA\text{-}PEG)}$, (d) $Ni_{10(OP)}/CaO_{(TF)}$. An offset was made along the y-axis for the sake of clarity.

The NiO crystallite sizes are much smaller (12 and 9 nm, respectively) in the materials obtained by hydrothermal autoclave synthesis ($Ni_{5(OP)}/CaO_{(HA\text{-}PEG)}$ and $Ni_{5(OP)}/CaO_{(HA\text{-}CTAB)}$) (Table 1). In addition to their higher porosity, this might be explained by the fact that nickel was present in the synthesis gel from the very first step of preparation, favouring homogeneous nickel mixing within the oxide support.[10,12] More strikingly, despite the relatively high Ni loading in $Ni_{10(TS)}/CaO_{(HT)}$ prepared by hard template method, XRD peaks attributable to NiO nanoparticles are hardly observed, suggesting average size of NiO crystallites below 4-5 nm (Fig. 2A, curve a), meaning that a good NiO dispersion (Table 1) was reached with this method. In addition, the presence of $CaCO_3$ is evidenced in some of the calcined samples (mainly those of the HA series), attested by a series of peaks at 2Θ equal to

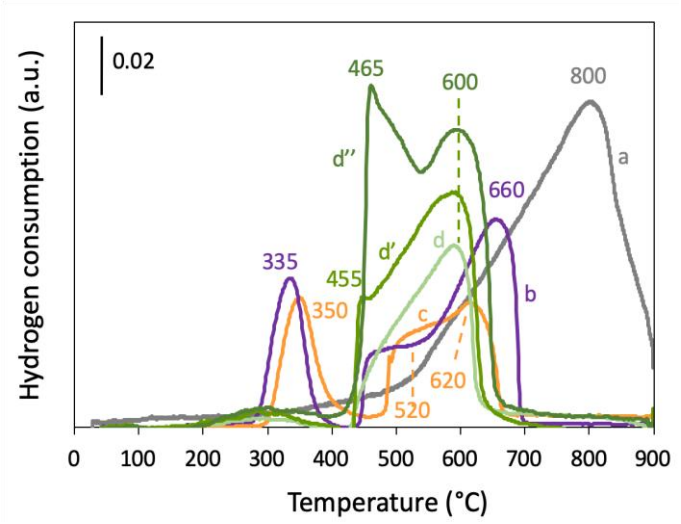

Figure 4: H_2-TPR profiles for calcined samples: (a) $Ni_{10(TS)}/CaO_{(HT)}$, (b) $Ni_{5(OP)}/CaO_{(HA-CTAB)}$, (c) $Ni_{5(OP)}/CaO_{(HA-PEG)}$, (d) $Ni_{5(OP)}/CaO_{(TF)}$, (d') $Ni_{7.5(OP)}/CaO_{(TF)}$ and (d'') $Ni_{10(OP)}/CaO_{(TF)}$.

19, 22, 29, 36, 39, 47, 48, 57, 58, 61, 64, 72 and 80°. Such $CaCO_3$ formation is attributable to the known basic properties of calcium oxide materials that can easily capture and store CO_2 from the atmosphere.

Reducibility of calcined samples

Finally, calcined materials were characterized with respect to their reducibility, identified from their H_2-TPR profiles (Fig. 4) and the related overall H_2 uptakes (Table 1). Regarding the three $Ni_{x(OP)}/CaO_{(TF)}$ samples obtained by template-free method, the one with the lowest Ni amount ($Ni_{5(OP)}/CaO_{(TF)}$) exhibits a single broad reduction peak at an intermediate temperature of 600 °C (Fig. 4, curve d). Such profile suggests some homogeneity among the NiO nanoparticles and a rather high degree of metal support interaction. For Ni-richer $Ni_{7.5(OP)}/CaO_{(TF)}$ (Fig. 4B, curve d') and $Ni_{10(OP)}/CaO_{(TF)}$ (Fig. 4, curve d''), another reduction peak appears at around 460 °C, with a relative intensity that increases with the Ni loading, indicating the increasing presence of more reducible nickel, interacting less strongly with the support. Similar reduction peaks take place for both $Ni_{5(OP)}/CaO_{(HA-CTAB)}$ (Fig. 4, curve b) and $Ni_{5(OP)}/CaO_{(HA-PEG)}$ (Fig. 4, curve c) prepared by hydrothermal autoclave synthesis but a third peak at low temperature also appears (at c.a. 340°C), suggesting the additional occurrence of weakly attached Ni-based nanoparticles. On the opposite, the reduction of $Ni_{10(TS)}/CaO_{(HT)}$ prepared by the hard template technique gives only one reduction peak at high temperature, with a maximum of H_2 uptake at 800 °C and a shoulder centered at 650 °C (Fig. 4, curve a). Such nickel reduction at high temperature (above 500°C) indicates the presence of strong metal support interaction. This fully agrees with the above conclusion (from XRD) of an extremely high nickel dispersion in this sample and is remarkable compared with the scarce literature available on NiO/CaO, only reporting a TPR peak centered around 415 °C until now.[19]

Importantly, the H_2-TPR profile of $Ni_{10(TS)}/CaO_{(HT)}$ (Fig. 4, curve a) confirms the expected

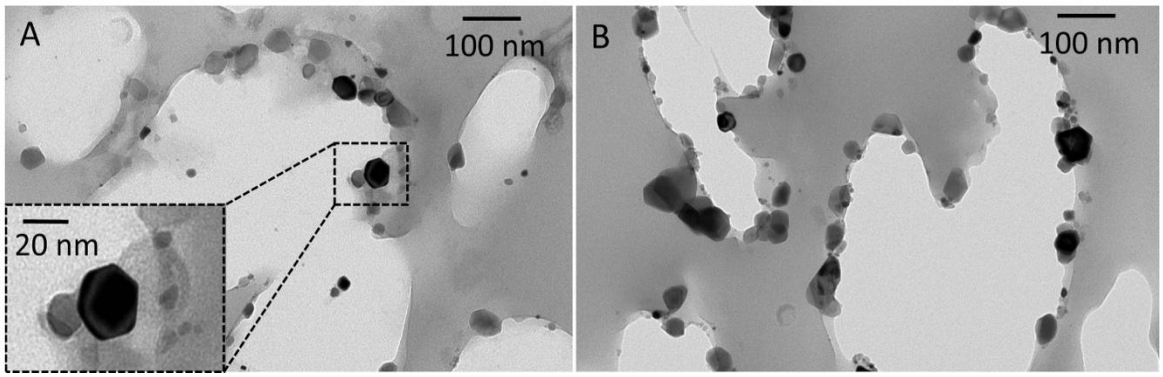

Figure 3: Ultrathin TEM micrographs of fresh (A) $Ni_{5(OP)}/CaO_{(TF)}$ and (B) $Ni_{10(OP)}/CaO_{TF)}$ prepared by template-free synthesis.

presence of nickel in the material prepared by hard template synthesis even if no NiO crystalline domains were detected by XRD (Fig. 2A, curve a), probably because of being too small. Furthermore, it is noteworthy that there is a good agreement between the amount of the H_2 consumption estimated from the area under the main reduction peak of the H_2-TPR profile and the expected Ni amount expressed in weight percent for all the investigated samples. Such good correlation confirms that the amount of nickel added during preparation was always recovered appropriately in the materials.

Performances of reduced catalysts in dry reforming of methane

Catalytic performances of the six materials were measured after *in-situ* reduction at atmospheric pressure under flowing 5%H_2/Ar at 700 °C for 2 h. The temperature was then decreased to 650 °C to conduct the activity and stability tests carried out for 13 h, at atmospheric pressure, under a CH_4:CO_2 ratio of 1:1 (diluted in 90% Ar) and a gas hourly space velocity GHSV of 36 L g_{cat}^{-1} h^{-1}. Methane and carbon dioxide conversions and molar H_2:CO ratios recorded as a function of time-on-stream are plotted on Fig. 5. For the sake of completion, and due to the different Ni contents in some catalysts, the apparent conversion rates of CH_4 and CO_2 were also evaluated (per g of Ni) and the obtained values are compared in Table 2 after 1 and 10 h of run.

Briefly, the best catalytic conversions were obtained on the Ni-richest $Ni_{10(TS)}/CaO_{(HT)}$, $Ni_{7.5(OP)}/CaO_{(TF)}$ and $Ni_{10(OP)}/CaO_{(TF)}$ catalysts prepared by hard template or template free pathway (Fig. 5A,B, curves a, d' and d"), intermediate ones were reached on $Ni_{5(OP)}/CaO_{(TF)}$ containing 5 wt.% Ni (Fig. 5A,B, curve d) and both $Ni_{5(OP)}/CaO_{(HA\text{-}CTAB)}$ and $Ni_{5(OP)}/CaO_{(HA\text{-}PEG)}$ with also 5 wt.% Ni and issued from hydrothermal autoclave synthesis were the less active (Fig. 5A and B, curves b and c).

Looking into more details, both less active catalysts ($Ni_{5(OP)}/CaO_{(HA\text{-}CTAB)}$ and $Ni_{5(OP)}/CaO_{(HA\text{-}PEG)}$) were also the most unstable and progressively deactivated, especially during the first hours of reaction. Moreover, the H_2:CO ratio, expected to be close to 1 in case of a high selectivity towards DRM ($CH_4 + CO_2 \rightarrow 2H_2 + 2CO$), was below 1 and it regularly decreased with time on stream, especially on $Ni_{5(OP)}/CaO_{(HA\text{-}PEG)}$ (Fig. 5C, curve c), while both activity and selectivity losses were less accentuated on $Ni_{5(OP)}/CaO_{(HA\text{-}CTAB)}$ (Fig. 5, curves b). Such deactivation associated to a low H_2:CO ratio is attributable to the occurrence of the reverse water gas shift side reaction (RWGS, $CO_2 + H_2 \rightarrow CO + H_2O$) that converts CO_2 and H_2 into CO and steam, the

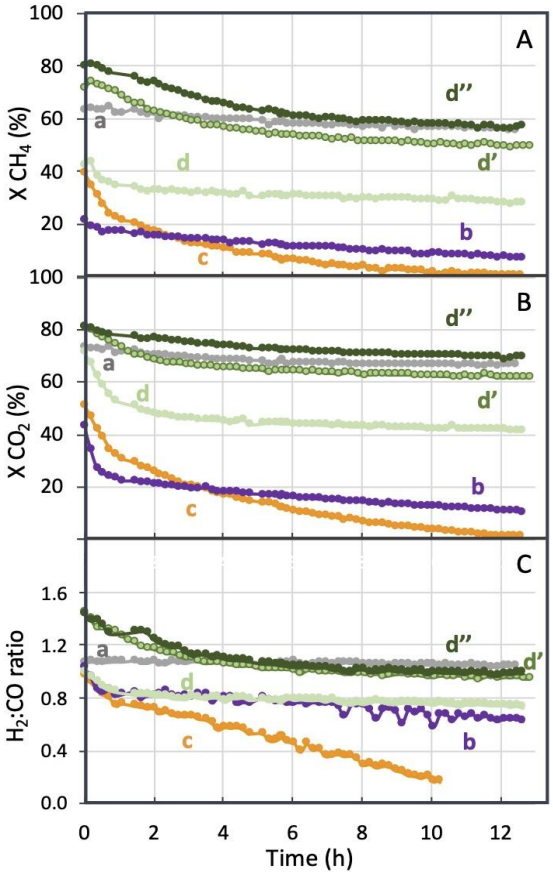

Figure 5: (A) CH_4 conversions, (B) CO_2 conversions and (C) H_2:CO ratio as a function of time (min) during dry reforming of methane (T=650 °C, P=1 atm, GHSV=36 L $gcat^{-1}$ h^{-1}) over in-situ reduced (a) $Ni_{10(TS)}/CaO_{(HT)}$, (b) $Ni_{5(OP)}/CaO_{(HA\text{-}CTAB)}$, (c) $Ni_{5(OP)}/CaO_{(HA\text{-}PEG)}$, (d) $Ni_{5(OP)}/CaO_{(TF)}$, (d') $Ni_{7.5(OP)}/CaO_{(TF)}$ and (d'') $Ni_{10(OP)}/CaO_{(TF)}$.

latter favoring nickel sintering.[47] RWGS as side reaction also explains the significantly higher CO_2 conversions compared to CH_4 ones (particularly in the first

hours of the run) as can be visualized in Figure 5 and from the comparison of CH_4 and CO_2 conversion rates in Table 2. This side reaction is favored in the range of 600-800 °C according to thermodynamic calculations performed using the HSC 7.1 Chemistry software.[44]

All the catalysts of the $Ni_{x(OP)}/CaO_{(TF)}$ series (with x = 5, 7.5 and 10 wt.% of Ni) were similarly unstable along the tests (Fig. 5 A and A', curves d, d' and d"). They were however more active than both above catalysts, including the one with same 5 wt.% Ni content (curve d, to be compared to curves b and c in Figure 5A and B). The extent of their deactivation during the 13 h test was moreover much more limited, of the order of 20%. Noticeably, the H_2:CO ratios in this case were higher than 1 (between 1.2 and 1.5) in the first hours, and then decreased down to values close to 1 at the end of the tests. Such high initial ratio values suggest that initial deactivation involves methane decomposition ($CH_4 \rightarrow C_{(s)} + 2H_2$, giving H_2 and carbon deposits). Nevertheless, the formed carbon does not seem to be strongly detrimental to overall Ni activity since the performances of the three catalysts are globally preserved after 12 h of test (even if to a lower extent on $Ni_{5(OP)}/CaO_{(TF)}$ on which the H_2/CO ratio tends to a value close to 0.8). The apparent conversion rates of both CH_4 and CO_2 reactants were also compared on this series of $Ni_{x(OP)}/CaO_{(TF)}$ catalysts (expressed per g of Ni, Table 2), leading to rate values systematically higher than for the other catalysts. This may be due to the contribution of side reactions increasing the conversion of reactants. The values were close for all 3 $Ni_{x(OP)}/CaO_{(TF)}$ catalysts after 10 h of run, independently of the Ni content, indicating a similar activity of the accessible Ni active sites, in agreement with the fact that the three materials were obtained by the same template free synthesis route and exhibit close physicochemical properties. Nevertheless, the comparison at initial state is more complex, with in particular a significantly higher r_{CH4} value for $Ni_{7.5(OP)}/CaO_{(TF)}$ than for $Ni_{10(OP)}/CaO_{(TF)}$ (Table 2). This can be explained by the fact that the initial methane conversions were high on both catalysts, close to thermodynamic equilibrium, and therefore maximum.[9-12] Then, part of the Ni active sites are no longer involved in the reaction due to a lack of reactants, and the effect should be accentuated in the catalysts with more nickel, thus leading to a lower rate when considering the activity per nickel site. The low r_{CH4} value for Ni-poor $Ni_{5(OP)}/CaO_{(TF)}$ is more unexpected

Table 2: Apparent conversion rates of methane (r_{CH4}) and carbon dioxide (r_{CO2}) at t=0 and t=10 hours during DRM stability tests (T=650 °C, P=1 atm, GHSV=36 L $gcat^{-1}$ h^{-1})

Catalyst	r_{CH4} * t=1 h	r_{CO2} * t=1 h	r_{CH4} * t=10 h	r_{CO2} * t=10 h
$Ni_{5(OP)}/CaO_{(TF)}$	1.4	2.1	1.2	1.7
$Ni_{7.5(OP)}/CaO_{(TF)}$	1.9	2.0	1.4	1.7
$Ni_{10(OP)}/CaO_{(TF)}$	1. 5	1.6	1.2	1.4
$Ni_{10(TS)}/CaO_{(HT)}$	1.2	1.4	1.2	1.4
$Ni_{5(OP)}/CaO_{(HA\text{-}PEG)}$	0.9	1.3	0.1	0.2
$Ni_{5(OP)}/CaO_{(HA\text{-}CTAB)}$	0.7	1.0	0.4	0.5

*: Conversion rates (in mmol s^{-1} g_{Ni}^{-1}) deduced from catalytic measurements.

but it could come from a certain degree of irreproducibility of the synthesis as suggested by the very big CaO crystals obtained in this sample (Table 1).

With respect to stability and selectivity, reduced $Ni_{10(TS)}/CaO_{(HT)}$ prepared by the hard template approach was definitely the best catalyst among the six tested materials, affording simultaneously high CH_4 and CO_2 conversions (59 and 68%, respectively), negligible activity losses, and high DRM selectivity (H_2:CO molar ratio around 1.04) (Fig. 5, curves a). This combined high activity and high stability can be attributed firstly to the high nickel dispersion, demonstrated by the very small size of the crystalline NiO domains before reduction (Fig. 2A, curve a), ensuring the presence in the reduced catalysts of numerous Ni^0 surface nickel sites able to activate the reactants. Secondly, in addition to favoring the metal dispersion, the high BET surface area (103 $m^2\ g^{-1}$) of this sample along with the presence of a porous network facilitates the accessibility of the reactants towards the Ni^0 active sites. Thirdly, the high metal support interaction attested by the high reduction temperature up to 800°C in the conditions of H_2-TPR (Fig. 4A, curve a) is known to enhance the resistance against metal sintering and carbon nanotubes formation).[9-11] It is also worth noting that the very good and stable performances of $Ni_{10(TS)}/CaO_{(HT)}$ indicate that the conditions of *in-situ* activation in 5%H_2/Ar at 700 °C for 2 h were well-adapted to successfully reduce NiO into Ni^0.

We may also hypothesize, as Wu et al.[45] did, that the efficient capture of CO_2 by the CaO supports, followed by its diffusion to the interface between CaO and the deposited Ni^0 nanoparticles, contributes to the good catalytic performances of the $Ni_{x(OP)}/CaO_{(TF)}$ and $Ni_{10(TS)}/CaO_{(HT)}$. Indeed, this could favor the oxidation of the intermediate activated carbon species arising from the CH_4 dissociation on the adjacent metallic nickel sites. To this respect, the high surface area of $Ni_{10(TS)}/CaO_{(HT)}$, providing more sites for CO_2 adsorption, represents an additional advantage.

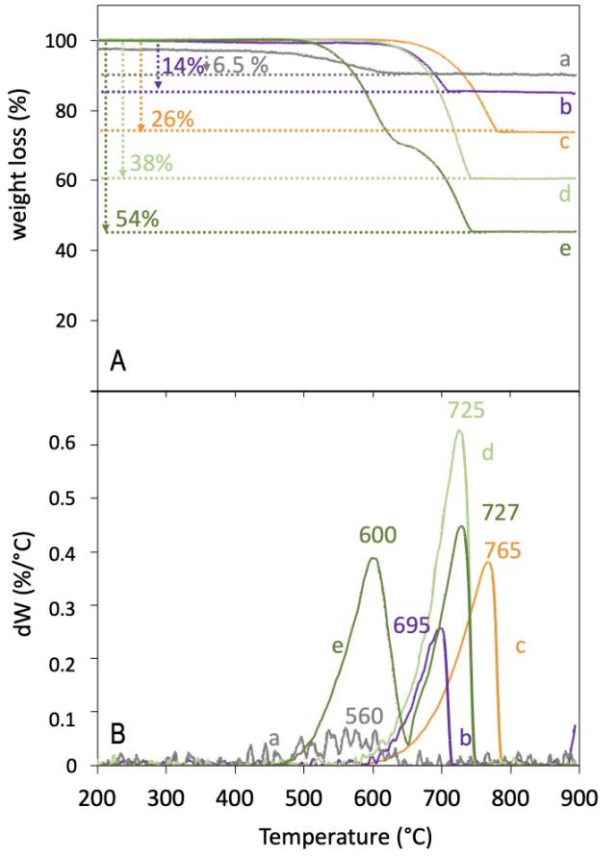

Figure 6: (A) TGA and (B) DTG profiles during heating in air of the spent catalysts: (a) $Ni_{10(TS)}/CaO_{(HT)}$, (b) $Ni_{5(OP)}/CaO_{(HA\text{-}CTAB)}$, (c) $Ni_{5(OP)}/CaO_{(HA\text{-}PEG)}$, (d) $Ni_{7.5(OP)}/CaO_{(TF)}$ and (e) $Ni_{10(OP)}/CaO_{(TF)}$

Characterization of spent catalysts

In order to provide additional understanding on stability behaviors, the catalysts recovered after tests were characterized by XRD (Fig. 2B) and TGA/DTG (Fig. 6), the latter analyses being conducted in order to qualify and quantify the carbonaceous deposits.

For $Ni_{10(OP)}/CaO_{(TF)}$, $Ni_{5(OP)}/CaO_{(HA\text{-}PEG)}$ and $Ni_{5(OP)}/CaO_{(HA\text{-}CTAB)}$, XRD peaks of metallic

Ni^0 with cubic structure were easily identified at 2Θ equal to 44, 51, and 76° (JCPDS 01-071-4653 file, Fig. 2B, curves b, c and d). Knowing that the densities of Ni and NiO are 8.9 and 6.7 g cm^{-3} respectively, one could expect a volumic size decrease of c.a. 40% in the absence of sintering during the reduction (i.e. in the reduced catalysts). The average Ni^0 sizes in the all series of spent $Ni_{x(OP)}/CaO_{(TF)}$ catalysts, as well as in $Ni_{10(TS)}/CaO_{(HT)}$, compared to those before reduction (Table 1), agree quite well with this estimation, suggesting a rather good stability of the nickel nanoparticles. On the contrary, the sizes increase is very important in both spent $Ni_{5(OP)}/CaO_{(HA\text{-}PEG)}$ (55 nm) and $Ni_{5(OP)}/CaO_{(HA\text{-}CTAB)}$ (109 nm), revealing a severe nickel sintering. The latter could have started during reduction but it occurred most probably mainly in the presence of steam during deactivation accentuated by the RWGS side reaction. On these aspects, a precise understanding of the exact processes taking place would require additional work. For spent $Ni_{10(TS)}/CaO_{(HT)}$, the Ni^0 diffraction peaks are still difficult to observe (Fig. 2B, curve a) due to their low intensity and broadening, indicative of the preserved small Ni^0 sizes (estimated around 6-8 nm).

In addition, the peaks at 2Θ equal to 23, 29, 36, 39, 43, 47, 48, 57, 61, 64, 66, 67, 73 and 82° detected in most of the XRD patterns of the spent catalysts are attributed to $CaCO_3$ nanoparticles with rhombohedral structure (JCPDS 01-080-2801 file). Their average sizes vary from 45 nm for $Ni_{5(OP)}/CaO_{(HA\text{-}PEG)}$ to 63 nm for $Ni_{10(OP)}/CaO_{(TF)}$. The formation of $CaCO_3$ nanoparticles during the DRM reaction is not surprising in view of the presence of CO_2 as a reactant during DRM, able to react with CaO. In addition, there are still few peaks of CaO detected at 2Θ equal to 32, 38, and 54° that are compatible with a cubic structure (JCPDS 01-077-2010 file). It is worth to mention that neither CaO nor $CaCO_3$ characteristic X-Ray diffraction peaks could be evidenced in the spent form of $Ni_{10(TS)}/CaO_{(HT)}$, suggesting again an excellent stability of this catalyst, not only with respect to the nickel active phase but also in term of preservation after reduction and test of the small size of the calcium oxide grains constituting the support.

TGA along with DTG profiles obtained between 300 and 900 °C during calcination in air flow of four representative spent samples (Fig. 6A and B) were used, in complement to XRD patterns (Fig. 2B), to characterize and quantify the carbon deposits in the spent catalysts. The quantity of deposited carbon was the smallest (of the order of 6.5 wt.%) in spent $Ni_{10(TS)}/CaO_{(HT)}$ prepared by hard template synthesis, while it was around 14 wt.% in spent $Ni_{5(OP)}/CaO_{(HA\text{-}CTAB)}$, 26 wt.% in spent $Ni_{5(OP)}/CaO_{(HA\text{-}PEG)}$, 38% in spent $Ni_{7.5(OP)}/CaO_{(TF)}$ and as high as 54 wt.% in spent $Ni_{10(OP)}/CaO_{(TF)}$ prepared by template-free synthesis. The high carbon amounts in spent $Ni_{7.5(OP)}/CaO_{(TF)}$ and $Ni_{10(OP)}/CaO_{(TF)}$ fit the easy detection of the graphite peak at 2Θ = 26° on the corresponding XRD patterns (Fig. 2B, curve d for $Ni_{10(OP)}/CaO_{(TF)}$ and data not shown for $Ni_{7.5(OP)}/CaO_{(TF)}$). They agree with the afore mentioned assumption of methane decomposition taking place on these two catalysts during the first hours of reaction, giving H_2:CO molar ratio higher than 1 (Fig. 5C, curves d' and d"). Similarly, the small amount of carbon deposited on $Ni_{10(TS)}/CaO_{(HT)}$ (6.5 wt.%) agrees with the absence of X-Ray diffraction carbon peak at 26° (Fig. 2B, curve a) and with the H_2:CO ratio constantly close to 1 during DRM (Fig. 5C, curve a). Note that this carbon content is very small compared to the value of 44 wt.% reported by Choudhary *et al.* in one of the rare published papers on Ni-based CaO catalysts for a 10 wt.% Ni/CaO catalyst.[19] This highlights the good resistance of $Ni_{10(TS)}/CaO_{(HT)}$

to coke deposition which is directly related to the beneficial synthetic approach followed to produce this catalyst with enhanced physicochemical properties: high BET surface area of 103 $m^2 g^{-1}$, high Ni dispersion (seen by XRD), high metal-support interaction (seen by H_2–TPR) and low sensitivity to carbon deposition, probably involving the positive effect of the basic CaO metal oxide providing oxygen atoms able to oxidize the carbon atoms generated by the decomposition of methane.

With respect to carbonaceous deposits, three main types are usually reported, i.e. amorphous Cα of low stability, Cβ and crystalline Cγ graphite. They are conventionally oxidized in the temperature ranges between 300 to 450 °C, 450 to 550 °C, and above 550 °C, respectively.[44,47] The spent $Ni_{10(OP)}/CaO_{(TF)}$ catalyst with the highest carbon amount, was characterized by two TGA weight losses at 600 and 727°C (Fig. 6B, curve e), revealing the presence of mainly Cγ carbon types (inert coke) that encapsulates part of the Ni metal species and lead to catalytic deactivation. Such coke is also present in $Ni_{7.5(OP)}/CaO_{(TF)}$ (TGA peak at 725°C). These results confirm again the correlation between carbon deposits formation and the deactivation observed on both $Ni_{7.5(OP)}/CaO_{(TF)}$ and $Ni_{10(OP)}/CaO_{(TF)}$ in the first hours of the tests. After that, $Ni_{10(OP)}/CaO_{(TF)}$ and $Ni_{7.5(OP)}/CaO_{(TF)}$ continue to be active, selective and stable due to a significant amount of accessible Ni metal species remaining unaffected by the carbon deposition. For both $Ni_{5(OP)}/CaO_{(HA\text{-}CTAB)}$ and for $Ni_{5(OP)}/CaO_{(HA\text{-}PEG)}$, the TGA peaks are also positioned at high temperatures, i.e. 710 °C and 775 °C, respectively, indicating again the presence of crystalline Cγ graphite with a high poisoning effect that strongly contributes to the total deactivation of both catalysts. On the contrary, the shift to a lower temperature (540 °C) of the TGA peak for $Ni_{10(TS)}/CaO_{(HT)}$ (Fig. 6B, curve a) reveals the presence of Cβ $C_{(s)}$ nanotubes, which are reported to be non-detrimental towards catalytic stability.[15] This explains the higher stability and good activity of this catalyst during the 13 h of DRM test.

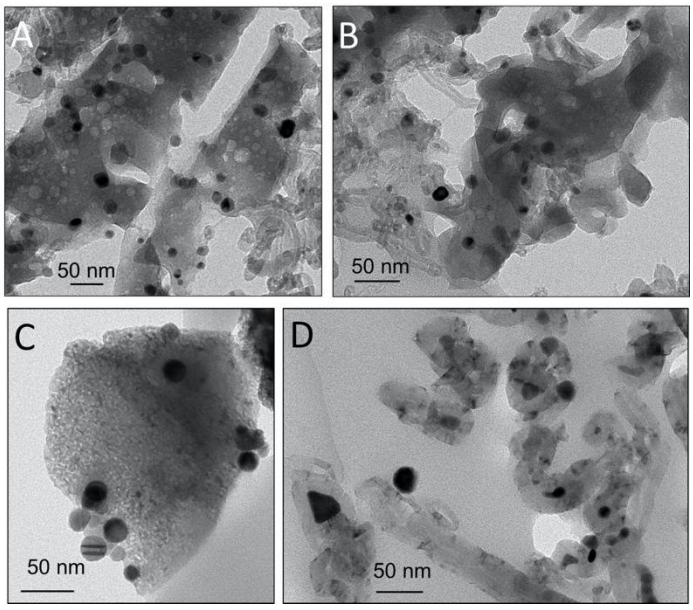

Figure 7: Ultrathin TEM micrographs of spent spent (A, B) $Ni_{10(TS)}/CaO_{(HT)}$, (C) $Ni_{5(OP)}/CaO_{(TF)}$ and (D) $Ni_{10(OP)}/CaO_{(TF}$ catalysts.

For the sake of completion, the spent forms of some of the catalysts, i.e. $Ni_{5(OP)}/CaO_{(TF)}$, $Ni_{10(OP)}/CaO_{(TF)}$ and $Ni_{10(TS)}/CaO_{(HT)}$, were characterized by TEM (Fig. 7). The representative micrograph shown for $Ni_{5(OP)}/CaO_{(TF)}$ attests of the presence of accessible Ni^0 metal nanoparticles with negligible carbon deposition (Fig 7C). Few carbon filaments are detected in spent $Ni_{10(OP)}/CaO_{(TF)}$ (Fig. 7D), in line with its higher Ni metal loading, giving higher methane conversion (favorable to carbon deposits), but Ni nanoparticles encapsulated by carbon (graphite) are also visible, explaining further the initial small deactivation. Again, the presence

of a significant number of active Ni^0 metal species not affected by the carbon formed ensures a high activity, selectivity and stability of the catalyst after 13 h (Fig. 5A, B, and C curve d'). For spent $Ni_{10(TS)}/CaO_{(HT)}$, Fig. 7A and 7B show mainly carbon filaments formed on the surface. This type of carbon identified as Cβ from TGA (Fig. 6A and 6B, curves a) is reported to have no poisoning effect on the catalytic activity, in good accordance with the good catalytic stability of this catalyst.

Conclusion

In comparison with MgO, porous CaO materials with reasonable textural properties are poorly described in the literature despite their strong interest as non-innocent supports in heterogeneous catalysis. In this contribution, CaO materials with up to 100 $m^2\ g^{-1}$ surface area and different nickel loadings were synthesized according to three synthetic approaches, based on either a template-free (TF) protocol (starting from ordered mesoporous calcium carbonate), a hard template (HT) protocol (involving SBA-15 silica), or a hydrothermal autoclave (HA) synthesis protocol (with structure directing agents PEG1500 or CTAB). The novelties in the implemented protocols lie in the use of Upsalite (mesoporous calcium carbonate) as a starting material (TF approach), of SBA-15 silica (HT approach) and of PEG1500 and CTAB as structure directing agents (HA syntheses). Depending on the protocol, nickel (5, 7.5 and 10 wt.%) was introduced by a "two-solvents" impregnation (HT series) or by incorporating the nickel source in the synthesis gel (TF and HA series). The three preparation procedures were adopted with the aim to produce Ni/CaO catalysts with high porous texture and robust structure to be investigated under the conditions of dry reforming of methane (here, at 650 °C for 13 h under a gas hourly space velocity of 36 L $g_{cat}^{-1}\ h^{-1}$).

The best physicochemical as well as catalytic properties were obtained by the hard-template route that led to a mesoporous $Ni_{10(TS)}/CaO_{(HT)}$ material with unusually high specific surface (103 $m^2\ g^{-1}$) and pore volume (0.50 mL g^{-1}) for CaO-based solids. Moreover, nickel was finely dispersed and stabilized over the support, giving after reduction a stable and selective DRM catalyst. High activity levels were also reached on the two Ni-rich catalysts $Ni_{10(OP)}/CaO_{(TF)}$ and $Ni_{7.5(OP)}/CaO_{(TF)}$ prepared by the template-free approach that presents several advantages over the hard template one, by being a new, easy, scalable, and time saving method of low energy requirements. However, the catalysts were then much more sensitive to deactivation and suffered from the formation of important carbon deposits. They moreover appeared as non-porous and relatively big (50 to 150 nm in size) CaO-based grains with poorly dispersed nickel-based nanoparticles (mean sizes around 20 nm). Finally, the hydrothermal autoclave synthesis results in non-stable and non-selective Ni-CaO materials that deactivate rapidly from the beginning of the test due to the occurrence of a severe sintering and RWGS side reaction.

As a whole, this work demonstrates that porous and high surface area CaO based materials can be synthesized and used as efficient supports of metal active nanoparticles such as nickel for catalytic application in demanding reactions like the dry reforming of methane.

Conflicts of interest

There are no conflicts to declare

Acknowledgements

The authors sincerely acknowledge the ERANET EU-FP7 initiative, the national ANR (France) and CNRS-L (Lebanon) agencies for their financial support through the SOL-CARE (Energy-065) project (JC-ENERGY-2014 first call). The University of Balamand Research Council is also thanked for the BIRG 02/2016 contribution.

References

1 D. Gu and F. Schüth, *Chemical Society Reviews*, 2014, **43**, 313-344.

2 J. C. Védrine, *ChemSusChem*, 2019, **12(3)**, 577-588.

3 J. C. Védrine, *Metal oxides in heterogeneous catalysis*, Ed. G.S. Korotcenkov, Elsevier, 2018.

4 CB&I Catofin® Process Brochure, Website: *https://www.cbi.com/getattachment/9c663848-b4ae-4c51-b51a 49db1154c47f/CATOFIN-Dehydrogenation.aspx,* 2014

5 J. Deng, L. Zhang, C. Liu, Y. Xia and H. Dai, *Catalysis Today*, 2011, **164**, 347-352.

6 A. Akgsornpeak, T. Witoon, T. Mungcharoen and J. Limtrakul, *Chemical Engineering Journal*, 2014, **237**, 189-198.

7 F. Meshkani, M. Rezaei and M. Andache, *Journal of Industrial and Engineering Chemistry*, 2014, **20**, 1251-1260.

8 L. Karam, S. Casale, H. El Zakhem and N. El Hassan, *Journal of CO_2 Utilization*, 2017, **17**, 119-124.

9 M. N. Kaydouh, N. El Hassan, A. Davidson, S. Casale, H. El Zakhem and P. Massiani, *Microporous and Mesoporous Materials*, 2016, **220**, 99-109.

10 L. Karam, J. Reboul, N. El Hassan, J. Nelayah and P. Massiani, *Molecules*, 2019, **24(22)**, 4107.

11 O. Daoura, G. El Chawich, M. Boutros, N. El Hassan, P. Massiani, O. Ersen, W. Baaziz, F. Launay, *Catalysis Communications*, 2020, **138**, 105953.

12 L. Karam, J. Reboul, S. Casale, P. Massiani and N. El Hassan, *ChemCatChem*, 2020, **12(1)**, 373-385.

13 O. Daoura, S. Daher, M.N. Kaydouh, N. El Hassan, P. Massiani, F. Launay and M. Boutros, *International Journal of Hydrogen Energy*, 2018, **43(36)**, 17205-17215.

14 Y. Sun, G. Zhang, J. Liu, Y. Xu and Y. Lv, *International Journal of Hydrogen Energy*, 2020, ***45*(1)**, 640-649.

15 N. D. Charisiou, L. Tzounis, V. Sebastian, S. J. Hinder, M. A. Baker, K. Polychronopoulou, M. A. Goula, *Applied Surface Science*, 2019, **474**, 42-56.

16 Y. Song, E. Ozdemir, S. Ramesh, A. Adishev, S. Subramanian, A. Harale, M. Albuali, B. Abdullah Fadhel, A. Jamal, D. Moon, S. H. Choi and C. T. Yavuz, *Science*, 2020, **367(6479)**, 777-781.

17 A. A. Lemonidou and I. A. Vasalos, *Applied Catalysis A: General*, 2002, **228**, 227-235.

18 A. Cruz-Hernández, J. A. Mendoza-Nieto and H. Pfeiffer, *Journal of Energy Chemistry*, 2017, **26**, 942-947.

19 V. R. Choudhary and A. M. Rajput, *Industrial & Engineering Chemistry Research*, 1996, **35**, 3934-3939.

20 W. D. Zhang, B. S. Liu and Y. L. Tian, *Catalysis Communications*, 2007, **8**, 661-667.

21 C. Liu, L. Zhang, J. Deng, Q. Mu, H. Dai and H. He, *The Journal of Physical Chemistry C*, 2008, **112**, 19248-19256.

22 A. Ebrahimi, M. Arab, M. Saffari, A. I. Minett and T. Langrish, *Chemical Engineering Journal*, 2016, **291**, 1-11.

23 H. R. Radfarnia and A. Sayari, *Chemical Engineering Journal*, 2015, **262**, 913-920.

24 W. C. Li, A. H. Lu, C. Weidenthaler and F. Schüth, *Chemistry of materials*, 2004, **16**, 5676-5681.

25 J. Roggenbuck, G. Koch and M. Tiemann, *Chemistry of Materials*, 2006, **18**, 4151-4156.

26 I. Zamboni, C. Courson and A. Kiennemann, *Applied Catalysis B: Environmental*, 2017, **203**, 154-165.

27 Y. B. Cho, G. Seo and D. R. Chang, *Fuel Processing Technology*, 2009, **90**, 1252-1258.

28 M. Kouzu, T. Kasuno, M. Tajika, Y. Sugimoto, S. Yamanaka and J. Hidaka, *Fuel*, 2008, **87**, 2798-2806.

29 M. Kouzu, S. Y. Yamanaka, J. S. Hidaka and M. Tsunomori, *Applied Catalysis A: General*, 2009, **355(1-2)**, 94-99.

30 H. Lu, A. Khan and P. G. Smirniotis, *Industrial & Engineering Chemistry Research*, 2008, **47**, 6216-6220.

31 O. Cheung, P. Zhang, S. Frykstrand, H. Zheng, T. Yang, M. Sommariva and M. Strømme, *RSC Advances*, 2016, **6**, 74241-74249.

32 J. Forsgren, S. Frykstrand, K. Grandfield, A. Mihranyan and M. Strømme, *PLoS One*, 2013, **8**, e68486.

33 S. Frykstrand, J. Forsgren, A. Mihranyan, and M. Strømme, *Microporous and Mesoporous Materials*, 2014, **190**, 99-104.

34 J. Yang, Y. Han, J. Luo, K. Leifer, M. Strömme and K. Welch, *Materials Chemistry and Physics*, 2019, **224**, 301-307.

35 S. Yamanaka, T. Oiso, Y. Kurahashi, H. Abe, K. Hara, T. Fujimoto and Y. Kuga, *Journal of Nanoparticle Research*, 2014, **16**, 2266.

36 M. Imperor-Clerc, D. Bazin, M. D. Appay, P. Beaunier and A. Davidson, *Chemistry of Materials*, 2004, **16**, 1813-1821.

37 K.S.P. Karunadasa, C.H.Manoratne, H.M.T.G.A.Pitawala, R.M.G.Rajapakse, *Journal of Physics and Chemistry of Solids*, 2019, **134**, 21-28.

38 I. Lopes, N. El Hassan, H. Guerba, G. Wallez and A. Davidson, *Chemistry of Materials*, 2006, **18**, 5826-5828.

39 C. Ettarh, A.K. Galwey, *Thermochimica Acta*, 1996, **288(1-2)**, 203-219.

40 M. Thommes, K. Kaneko, A. V. Neimark, J. P. Olivier, F. Rodriguez-Reinoso, J. Rouquerol and K. S. Sing, *Pure and Applied Chemistry*, 2015, **87**, 1051-1069.

41 S. G. Hosseini, R. Ahmadi, A. Ghavi and A. Kashi, *Powder Technology*, 2015, **278**, 316-322.

42 M. Thommes, *Chemie Ingenieur Technik*, 2010, 82, 1059-1073.

43 K. S. Sing, *Pure and Applied Chemistry*, 1985, **57**, 603-619.

44 K. Jabbour, P. Massiani, A. Davidson, S. Casale and N. El Hassan, *Applied Catalysis B: Environmental*, 2017, **201**, 527-542

45 P. Wu, Y. Tao, H. Ling, Z. Chen, J. Ding, X. Zeng, X. Liao, C. Stampfl and J. Huang, *ACS Catalysis*, 2019, **9**, 10060-10069.

46 F. Meshkani, M. Rezaei and M. Andache, *Journal of Industrial and Engineering Chemistry*, 2014, **20**, 1251-1260.

47 K. Jabbour, A. Saad, L. Inaty, A. Davidson, P. Massiani and N. El Hassan, *International Journal of Hydrogen Energy*, 2019, **44**, 14889-14907.